

All-Optically Controlled Topological Transistor Based on Xenes

Jun Zheng^{1,2,*}, Yang Xiang,³ Chunlei Li,^{2,4} Ruiyang Yuan,⁵ Feng Chi,⁶ and Yong Guo^{2,7,†}

¹School of Mathematics and Physics, Bohai University, Jinzhou 121013, China

²Department of Physics and State Key Laboratory of Low-Dimensional Quantum Physics, Tsinghua University, Beijing 100084, China

³College of New Energy, Bohai University, Jinzhou 121013, China

⁴College of Elementary Education, Capital Normal University, Beijing 100048, China

⁵Center for Theoretical Physics, Department of Physics, Capital Normal University, Beijing 100048, China

⁶School of Electronic and Information Engineering, University of Electronic Science and Technology of China
Zhongshan Institute, Zhongshan 528400, China

⁷Collaborative Innovation Center of Quantum Matter, Beijing 100084, China

(Received 26 January 2020; revised 7 June 2020; accepted 27 July 2020; published 10 September 2020)

We theoretically propose an X ene ($X = \text{Si}, \text{Ge}$, or Sn) transistor that can be operated with high and low threshold light parameters. The results reveal that a spin-dependent nonconductive path in the X ene superlattice can be formed by utilizing an off-resonant light-induced topological phase transition and the band mismatch between illuminated and unilluminated regions. This topological transistor can be switched between an *on* state with a 100% spin-polarized weak current, an *on* state with a nonpolarized strong current, and an *off* state with a controllable breakdown voltage, just by adjusting the polarization state of circularly polarized light. With the assistance of an electric field, the X ene transistor can be operated at low light parameters, the threshold parameter of the transistor can be reduced to much lower than the spin-orbit coupling strength, and the breakdown voltage can be larger than the bulk band gap of the unilluminated X ene. All the results indicate that the proposed X ene nanosystems are promising candidates for topological electronic devices.

DOI: 10.1103/PhysRevApplied.14.034027

I. INTRODUCTION

Since the successful fabrication of graphene [1], two-dimensional materials have been evolving at a rapid pace and are considered ideal candidates for next-generation electronics and optoelectronics [2,3]. Following success with single layers of carbon atoms, the corresponding monolayers of other group-IVA atoms (from Si to Pb) have been proposed in theory [4–10] and successfully synthesized in experiments [11–18]. All the group-IVA monolayer materials have a similar hexagonal lattice structure along the [001] direction, and hence possess a high electron mobility and thermal conductivity. In contrast to graphene, the monolayers from silicene to plumbene consist of heavier atoms, such that the spin-orbit coupling is large enough to open a fully insulating bulk band gap at the

Dirac points and lead to time-reversal-symmetry-protected metallic states at edges [19]. These edge states are unique in that the spin and momentum are locked and that backward scattering is forbidden in the absence of magnetic impurities [20,21]. For pristine silicene, germanene, and stanene, helical edge states are found at the Γ point in the Brillouin zone [22], while for plumbene other local topological states are formed at the k/k' point with the p_z orbital [23]. Therefore, among the group-IVA monolayer materials, the pristine X enes ($X = \text{Si}, \text{Ge}$, or Sn) show features of a topological insulator.

The hybridization of Si, Ge, or Sn atoms in the process of forming a monolayer favors sp^2 and sp^3 mixed bonding [4,7], and consequently the buckled X enes are more stable than the planar ones. The buckled structure, with a layer separation between the two sublattices, allows one to change the effective mass of the charge carriers and tune the band gap by applying an electric field in the perpendicular direction [24–27]. Based on the above properties, electric-field-controlled topological transistors have received significant attention [28–35].

In transistors [36], the *on-off* switches that make computing digital are the core of integrated circuits and the basis of various electronic devices. In most mainstream

*junzheng@semi.ac.cn

†guoy66@tsinghua.edu.cn

Published by the American Physical Society under the terms of the Creative Commons Attribution 4.0 International license. Further distribution of this work must maintain attribution to the author(s) and the published article's title, journal citation, and DOI.

logic and memory chips, billions of transistors are interconnected through copper wires on the wafer that are several nanometers wide. An enormous amount of heat, which not only causes significant energy consumption but also limits the integration density and processing speed of the chip, is generated as billions of transistors switch and shuttle data [37,38]. How to solve the overheating problem is an essential topic for both current and future electronics. A topological-insulator transistor is robust against impurities and randomness because of topological protection [20,21]. Using topological transistors to replace ordinary transistors would effectively limit electron collisions and self-heating. In addition, because the interaction between photons is extremely weak, photons can transmit information for a long time while maintaining low signal degradation and low power dissipation. Using photons as signal carriers and replacing metal interconnects with optical interconnects can further reduce heat generation in nanoscale integrated circuits [39].

Compared with field-effect transistors manipulated by an electric field, optically controlled transistors perform the function of an output-current modulator with the electric field inputs replaced with light-field inputs or with extra light-field inputs added. In recent years, photoinduced transistors have been investigated both theoretically and experimentally based on various two-dimensional nanostructures, such as graphene, molybdenum disulfide, and black phosphorus [40–44]. In this paper, we propose a topological transistor consisting of an *Xene* nanoribbon in the presence of circularly polarized light. As shown in Fig. 1, the center area of the device is divided into two parts, and a pair of circularly polarized light beams irradiate the sheet. Some areas of the nanoribbon are periodically covered with an opaque material, thus forming a periodic superlattice structure illuminated and not illuminated by light. In the following, we discuss how to convert optical signals into different forms of electrical signals in *Xenes* by adjusting only the light parameters.

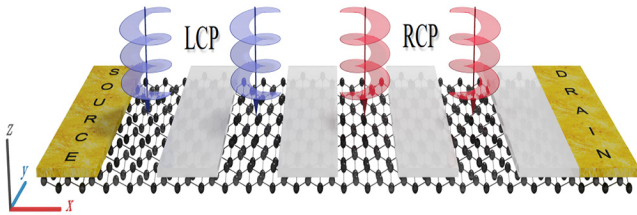


FIG. 1. (a) Schematic representation of *Xene* transistor decomposed into source electrode, central device, and drain electrode. Four areas of the central nanoribbon are covered periodically by areas of a nontransparent material with length $N_x = 5$ and width $N_y = 20$; the central device region is divided into two parts, and a pair of circularly polarized light beams irradiate it. LCP, left-circularly-polarized; RCP, right-circularly-polarized.

II. MODEL AND METHODS

The tight-binding Hamiltonian for electrons in the source (H_S), drain (H_D), and unilluminated central (H_C^{Dark}) *Xene* regions can be expressed as [45–49]

$$\begin{aligned} H_C^{\text{Dark}} = H_S = H_D = -t_X \sum_{\langle ij \rangle, \sigma} (a_{i\sigma}^\dagger b_{j\sigma} + \text{H.c.}) \\ + i \frac{\lambda_{\text{SO}}^X}{3\sqrt{3}} \sum_{\langle\langle ij \rangle\rangle, \sigma} (\sigma v_{ij} a_{i\sigma}^\dagger a_{j\sigma} + \sigma v_{ij} b_{i\sigma}^\dagger b_{j\sigma} + \text{H.c.}), \end{aligned} \quad (1)$$

where $a_{i\sigma}^\dagger$ ($b_{j\sigma}$) creates (annihilates) an electron with spin σ at lattice site i (j) on sublattice A (B). The spin index $\sigma = +1$ ($\sigma = -1$) denotes spin-up (spin-down) electrons. The index $\langle ij \rangle$ ($\langle\langle ij \rangle\rangle$) means that the summation is over all nearest-neighbor (next-nearest-neighbor) sites, and t_X ($X = \text{Si, Ge, Sn}$) represents the nearest-neighbor hopping energy between different sublattices. The second term in Eq. (1) describes the effective spin-orbit coupling, with strength λ_{SO}^X . In the two-dimensional case, the site-dependent Haldane phase factor [50] v_{ij} becomes a sign function, and $v_{ij} = +1$ ($v_{ij} = -1$) if the next-nearest-neighbor hopping is counterclockwise (clockwise) around a hexagonal lattice [51]. Compared with the effective spin-orbit coupling, the intrinsic Rashba spin-orbit coupling associated with the next-nearest-neighbor hopping is a small constant. Thus, the influence of intrinsic Rashba spin-orbit coupling is ignored in the numerical calculation.

The central device regions, exposed to off-resonant circularly polarized light and electric fields, can be described by the following Hamiltonian [52]:

$$\begin{aligned} H_C^{\text{Light}} = i \frac{\lambda_\Omega}{3\sqrt{3}} \sum_{\langle\langle ij \rangle\rangle, \sigma} (v_{ij} a_{i\sigma}^\dagger a_{j\sigma} + v_{ij} b_{i\sigma}^\dagger b_{j\sigma} + \text{H.c.}) \\ - \lambda_E \sum_{i, \sigma} (a_{i\sigma}^\dagger a_{i\sigma} - b_{i\sigma}^\dagger b_{i\sigma}). \end{aligned} \quad (2)$$

The first term in Eq. (2) represents the Haldane interaction induced by the photoirradiation [53,54], where the light parameter λ_Ω is equal to $9t_X^2 \Lambda^2 / 4\hbar\Omega$. The light intensity is characterized by $\Lambda = eaA/h$, where e is the electron charge and a is the lattice constant. The corresponding electromagnetic potential at time τ is given by $\mathbf{A}(\tau) = (A \sin \Omega\tau, A \cos \Omega\tau)$, where the frequency of the light Ω is less than 0 (greater than 0) for left (right) circulation. In the simulation calculation, back gates are assumed to be added to the light-irradiated regions, and λ_E in the second term of Eq. (2) is the staggered sublattice potential induced by the electric field. If the two sublattice planes of the buckled structure are separated by a distance ℓ and a z -direction electric field $E_z(x, y)$ is applied, the staggered sublattice potential between the atoms at the A and B sites is given by $\lambda_E = \ell E_z(x, y)$.

The spin-dependent current flowing through the drain electrode can be expressed in Landauer-formula form as [55,56]

$$\begin{aligned} I_{D\sigma} &= \frac{e}{h} \int T_{SD\sigma} [f_S(\varepsilon) - f_D(\varepsilon)] d\varepsilon \quad (V_{\text{bias}} > 0), \\ &= \frac{e}{h} \int T_{DS\sigma} [f_S(\varepsilon) - f_D(\varepsilon)] d\varepsilon \quad (V_{\text{bias}} < 0), \end{aligned} \quad (3)$$

where $T_{SD\sigma} = \text{Tr}[\Gamma_{S\sigma} \mathbf{G}_\sigma^r \Gamma_{D\sigma} \mathbf{G}_\sigma^a]$ ($T_{DS\sigma} = \text{Tr}[\Gamma_{D\sigma} \mathbf{G}_\sigma^r \Gamma_{S\sigma} \mathbf{G}_\sigma^a]$) is the spin-dependent transmission coefficient of electrons from the source (drain) to the drain (source) electrode, with the linewidth function $\Gamma_{S(D)\sigma} = i(\Sigma_{S(D)\sigma}^r - \Sigma_{S(D)\sigma}^a)$. The retarded (advanced) self-energy function of electrode α can be obtained from $\Sigma_{\alpha\sigma}^{r(a)} = \mathbf{H}_{C\alpha} \mathbf{g}_{\alpha\sigma}^{r(a)} \mathbf{H}_{\alpha C}$, in which the Hamiltonian matrix $\mathbf{H}_{\alpha C}$ describes the coupling between electrode α and the central device region. The surface Green's function $\mathbf{g}_{\alpha\sigma}^{r(a)}$ can be calculated by the transfer-matrix or the Green's-function method [57,58]. The Green's function of the entire system is given by $\mathbf{G}_\sigma^r(\varepsilon) = [\varepsilon \mathbf{I} - \mathbf{H}_0 - \Sigma_{S\sigma}^r - \Sigma_{D\sigma}^r]^{-1} = [\mathbf{G}_\sigma^a(\varepsilon)]^\dagger$, in which \mathbf{H}_0 is the Hamiltonian matrix of the central region. $f_\alpha(\varepsilon) = [e^{(\varepsilon - \mu_\alpha)/k_B T} + 1]^{-1}$ in Eq. (3) is the Fermi function, where μ_α is the electrochemical potential of electrode α , k_B is the Boltzmann constant, and T is the equilibrium temperature of the system. In a numerical calculation, the influence of temperature-induced thermal fluctuations of the electrons on the electronic transport can be studied by adjusting the value of T . When we consider the effect of the bias voltage V_{bias} , the electrochemical potentials of the source and drain electrodes are fixed at $\mu_S = -\mu_D = eV_{\text{bias}}/2$, and $V_{\text{bias}} > 0$ and $V_{\text{bias}} < 0$ correspond to forward and reverse bias, respectively.

By transforming the creation and annihilation operators in Eqs. (1) and (2) to the Bloch representation by means of the Bloch-Wannier transformation, $a_{j_y\sigma} = (1/\sqrt{N_y}) \sum_{k \in BZ} a_{k\sigma} e^{-ikj_y}$ and $a_{j_y\sigma}^\dagger = (1/\sqrt{N_y}) \sum_{k \in BZ} a_{k\sigma}^\dagger e^{ikj_y}$, where j_y is the position of the lattice site along the y direction, the energy bands of the illuminated and unilluminated regions can be derived.

III. RESULTS AND DISCUSSION

In the numerical results presented below, the nearest-neighbor hopping energies t_X and effective spin-orbit coupling strengths λ_{SO}^X of the X enes are taken as $t_{Si} = 1.6$ eV and $\lambda_{SO}^{Si} = 3.9$ meV (silicene) [9], $t_{Ge} = 1.3$ eV and $\lambda_{SO}^{Ge} = 43$ meV (germanene) [9], and $t_{Sn} = 1.3$ eV and $\lambda_{SO}^{Sn} = 100$ meV (stanene) [10]. The length and width of the illuminated (unilluminated) regions are fixed at $N_x = 350$ and $N_y = 40$, respectively, and the number of opaque areas is fixed at 8. The equilibrium temperature of the system is set to 4.2 or 300 K. It should be pointed out that the influence of temperature-induced thermal fluctuations of

the electrons on the electronic transport is considered in the numerical calculation, but the influence of phonons is neglected, because the ballistic transport length of edge states can be of the order of micrometers [59]. An off-resonant circularly polarized light field is considered in the following simulations. For silicene, germanene, or stanene, the off-resonance condition is satisfied when $\hbar\Omega \gg t_X$, the lowest frequency is determined by the bandwidth $\hbar\Omega = 3t_X \approx 10^{15}$ Hz, and, for the intensity of light available in this frequency regime, Λ is typically less than 1 [52,54]. Taking stanene as an example, when $\Lambda = 0.5$ and $\hbar\Omega = 3t_{Sn}$, the off-resonance condition is satisfied, and a light parameter $\lambda_\Omega \approx 2\lambda_{SO}^{Sn} = 0.2$ eV can be achieved. With the rapid development of nanoprocessing technology, dynamic manipulation of the polarization, frequency, amplitude, and phase of optical fields has been realized in various subwavelength artificial nanostructures [60].

The central device region is divided into two parts (I and II, as shown in Fig. 1). If we consider the different effects of left-circularly-polarized (LCP) and right-circularly-polarized (RCP) light, there are four light-receiving scenarios, i.e., only LCP or RCP light irradiates the whole device area [see Figs. 2(a) and 2(b)], no light irradiates the device [see Fig. 2(c)], and parts I and II are exposed to LCP and RCP light, respectively [see Fig. 2(d)].

The drain currents I_D of the stanene transistor as a function of the bias voltage V_{bias} for the different illumination cases are plotted in Fig. 2(e). It is clearly shown that the stanene nanoribbon can act as a purely optically controlled transistor, the conductive (*on*) state can be switched to the nonconductive (*off*) state, and the output current can be modulated to show three different types of behavior by only a light field, as follows. (1) Under illumination with LCP (RCP) light [as illustrated in Figs. 2(a) and 2(b)] with the light parameter satisfying $\lambda_\Omega < -\lambda_{SO}^{Sn}$ ($\lambda_\Omega > \lambda_{SO}^{Sn}$), the optical transistor can efficiently filter spin-up (spin-down) electrons within a specific bias range around the Fermi energy; the drain current is 100% spin-polarized [see the red dashed line in Fig. 2(e)]. (2) When $|\lambda_\Omega| < \lambda_{SO}^{Sn}$, or in the absence of light ($\lambda_\Omega = 0$) [as illustrated in Fig. 2(c)], the drain current is non-spin-polarized ($I_{\uparrow} = I_{\downarrow}$), and increases linearly with the bias voltage V_{bias} [see the blue dashed-dotted line in Fig. 2(e)]. The current intensity in the bulk band gap is approximately twice the value in the case in which only LCP or RCP light is applied. (3) When LCP and RCP light with $|\lambda_\Omega| > \lambda_{SO}^{Sn}$ is applied to regions I and II simultaneously [as illustrated in Fig. 2(d)], the output current I_D is zero within the bias window $-|\lambda_\Omega - \lambda_{SO}^{Sn}| < V_{\text{bias}} < |\lambda_\Omega - \lambda_{SO}^{Sn}|$ [see the black solid line in Fig. 2(e)], and the transistor is turned off.

Figure 2(f) depicts the current-voltage characteristics of the silicene and germanene transistors in the *off* state. It can be seen from the figure that the breakdown voltage is related to the light parameter and the spin-orbit coupling strength. The breakdown voltage can be controlled

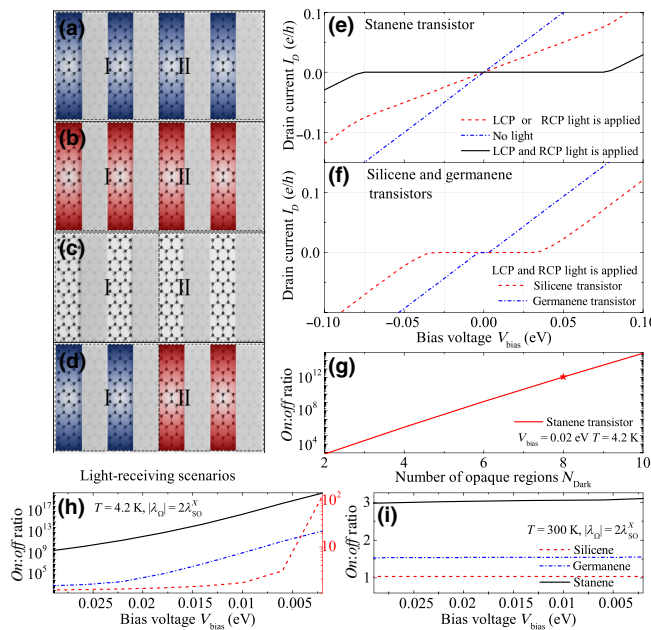


FIG. 2. Illustration of (a) LCP light ($\lambda_\Omega > 0$), (b) RCP light ($\lambda_\Omega < 0$), and (c) no light ($\lambda_\Omega = 0$) irradiating the entire device region. (d) Illustration of LCP and RCP light irradiating parts I and II, respectively, of the central device region. (e) Drain current of a stanene transistor as a function of the bias voltage V_{bias} with a light parameter $|\lambda_\Omega| = 2\lambda_{SO}^{Sn}$. (f) Drain current of silicene and germanene transistors in *off* state versus bias voltage V_{bias} with parameters $|\lambda_\Omega| = 2\lambda_{SO}^{Si}$ and $|\lambda_\Omega| = 2\lambda_{SO}^{Ge}$. (g) *On:off* ratio of stanene transistor versus number of opaque regions N_{Dark} at temperature $T = 4.2$ K and bias voltage $V_{bias} = 20$ meV. (h) *On:off* ratio of X ene transistor as a function of the bias voltage V_{bias} at 4.2 K. (i) *On:off* ratio versus V_{bias} at 300 K.

by the strength of the light parameter λ_Ω , and reaches its maximum value when $|\lambda_\Omega| = 2\lambda_{SO}^X$. Because the effective spin-orbit couplings of stanene and germanene are much larger than that of silicene, the breakdown voltages of stanene- and germanene-based transistors can reach tens of meV. Although the breakdown voltage of a silicene optically controlled transistor is only a few meV, it can exhibit a switching effect with a relatively weak light field.

The effect of the number of opaque regions N_{Dark} on the *on:off* ratio of the stanene transistor is depicted in Fig. 2(g). It is clearly shown that the *on:off* current ratio increases with the number of opaque regions. Because an increase in the length of a periodic structure can enhance the filtering effect for electrons, the *off* current nearly vanishes within the transmission window, and the *on:off* ratio is raised by a factor of 10^9 when N_{Dark} is increased from 2 to 8. A larger ratio is expected if the the number of opaque regions is increased further. Figures 2(h) and 2(i) show the drain-current *on:off* ratios of silicene, germanene, and stanene transistors at 4.2 and 300 K, respectively. It can be seen from Fig. 2(h) that the optically controlled transistors can maintain a good *off* state at low temperature,

the *on:off* ratios of the germanene and stanene transistors are obviously larger than that of the silicene transistor, and the *on:off* ratio of the stanene transistor can reach the order of 10^{12} under the condition of a 20-meV bias voltage. However, there is a significant reduction in the performance at room temperature [see Fig. 2(i)]. With an increase in temperature, thermal fluctuations cause higher-energy electrons to participate in transport, resulting in a significant increase in the *off* -state leakage current and a decrease in the *on:off* ratio.

To understand the transport properties of the optical transistor, here we take stanene ($\lambda_{SO}^{Sn} = 0.1$ eV) as an example and compare the energy-band diagrams of the unilluminated [see Fig. 3(a)] and illuminated [see Figs. 3(b)–3(d)] regions. As shown in Fig. 3(a), without an external light field ($\lambda_\Omega = 0$), the edge states form spin-degenerate Kramers doublets, the electron-transport direction is correlated with the spin, and the upper (lower) edge supports a forward (backward) mover with spin up and a backward (forward) mover with spin down. For $V_{bias} > 0$ ($V_{bias} < 0$), the spin-up (spin-down) electrons can tunnel from the left (right) electrode to the right (left) one through the upper edge state, while the spin-down (spin-up) electrons can be transported through the lower edge state; the quantum conductance of the edge modes is 2. Therefore, as shown by the blue dashed-dotted line in Fig. 2(e), the

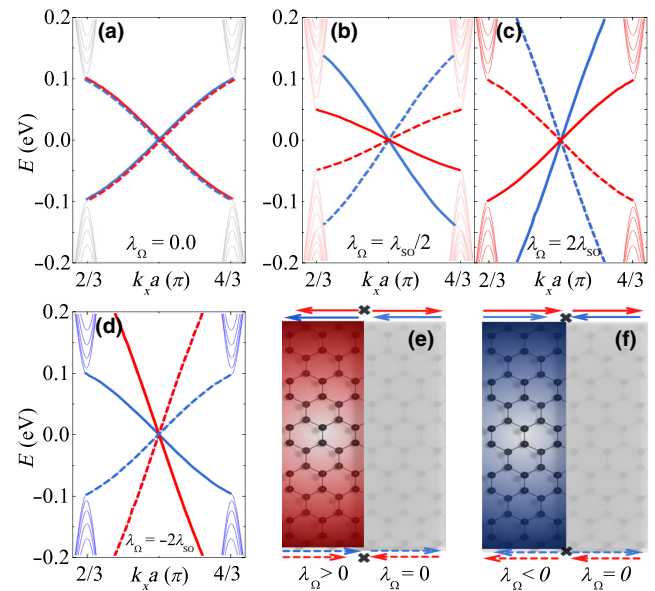


FIG. 3. (a)–(d) Energy-band diagrams of stanene with light parameters (a) $\lambda_\Omega = 0$, (b) $\lambda_\Omega = \lambda_{SO}^{Sn}/2$, (c) $\lambda_\Omega = 2\lambda_{SO}^{Sn}$, and (d) $\lambda_\Omega = -2\lambda_{SO}^{Sn}$. (e),(f) Schematic illustration of edge states in the real-space picture with (e) RCP ($\lambda_\Omega > \lambda_{SO}^{Sn}$) and (f) LCP ($\lambda_\Omega < -\lambda_{SO}^{Sn}$) light. The solid and dashed (red and blue) lines correspond to the upper and lower (spin-up and spin-down) edge states, respectively.

drain current I_D increases linearly with an increase in bias voltage V_{bias} with a slope of 2.

When a circularly polarized light field is applied and the second-order photocorrelation is considered, according to the Floquet theory the light does not directly excite electrons, but instead modifies the electron band structures through virtual photon-absorption processes. As shown in Fig. 3(b), if the light parameter satisfies the condition $-\lambda_{\text{SO}}^{\text{Sn}} < \lambda_{\Omega} < \lambda_{\text{SO}}^{\text{Sn}}$, the X ene is a quantum spin-Hall insulator, and the states at different edges are nondegenerate with different electron group velocities, but the spin-momentum locking and helical spin texture are still unchanged. If $|\lambda_{\Omega}| > \lambda_{\text{SO}}^{\text{Sn}}$, the X ene is transformed into a photoinduced quantum Hall insulator, the edge states transition from having a helical property to having an anisotropic chiral property, and the states with opposite spin propagate in only one direction at a given edge. For $\lambda_{\Omega} > +\lambda_{\text{SO}}^{\text{Sn}}$, the upper (lower) edge state supports both spin-up and spin-down electrons moving in the backward (forward) direction [see Fig. 3(c)]. For $\lambda_{\Omega} < -\lambda_{\text{SO}}^{\text{Sn}}$, however, the upper (lower) edge state supports forward (backward) movers [see Fig. 3(d)].

The spin-selective transport of electrons is induced by the edge-state mismatch between the illuminated [see Fig. 3(c)] and unilluminated [see Fig. 3(a)] regions. As illustrated in the real-space picture shown in Fig. 3(e), if the light parameter satisfies the condition $\lambda_{\Omega} > +\lambda_{\text{SO}}^{\text{Sn}}$, the upper (lower) edge supports transport both of spin-up and spin-down electrons along the $-x$ (x) axis. However, in the unilluminated region ($\lambda_{\Omega} = 0$), the upper edge supports spin-up (spin-down) electrons moving along the x ($-x$) direction, and conversely for the lower edge. The joint effect of the unilluminated regions and the regions illuminated with LCP (RCP) light makes the edge states support transport of only spin-up (spin-down) electrons within a certain range of bias voltage. Therefore, in the region of low bias, only one side of the edge is involved in electron transport when $V_{\text{bias}} > 0$ or $V_{\text{bias}} < 0$, the values of the charge current under the conditions $\lambda_{\Omega} = +2\lambda_{\text{SO}}^{\text{Sn}}$ and $\lambda_{\Omega} = -2\lambda_{\text{SO}}^{\text{Sn}}$ are the same, and the slope of the corresponding I - V curve is equal to 1 [see the red dashed line in Fig. 2(e)].

The state of the transistor switches from *on* to *off* when LCP and RCP light is applied to regions I and II, respectively. In this case, only spin-up electrons can tunnel through region I [see Fig. 3(e)], but it is hard for them to tunnel through region II [see Fig. 3(f)], and the conductive path in the X ene superlattice is blocked, leading to a strong reduction of the current, as shown in Figs. 2(e) and 2(f). Taking into account the fact that the spin-filtering and transistor action depends on the mismatch of the energy bands, the superlattice structure formed by periodically illuminated and unilluminated regions guarantees a better *off* state of the transistor. In addition to the edge-state phase transition, the light field can also affect the bulk band

gap of the X ene, and the bulk band gap in the presence of the light field becomes $2|\lambda_{\text{SO}} - \lambda_{\Omega}|$. Thus, the breakdown voltage of the transistor can be manipulated by the strength of the light parameter and reaches a maximum when $|\lambda_{\Omega}| = 2\lambda_{\text{SO}}$.

The metal-oxide-semiconductor field-effect transistor (MOSFET) is a type of insulated-gate field-effect transistor that is fabricated by controlled oxidation of a semiconductor [61]. The voltage on the covered gate determines the electrical conductivity of the device, and this ability to change the conductivity with the size of the applied voltage can be used for switching electrical signals. Since MOSFETs can be made with either *p*-type or *n*-type semiconductors, complementary pairs of MOSFETs are widely used as switching elements in logic circuits, in which an *n*-channel (*p*-channel) MOSFET acts as an open switch with a low (high) threshold gate voltage [62]. Because the threshold light parameters of silicene, germanene, and stanene transistors are different, when one is designing logic circuits, silicene and germanene transistors that can be turned off with lower light parameters can play a role similar to that of an *n*-channel depletion-type MOSFET, while stanene transistors can play a role similar to that of a *p*-channel depletion-type MOSFET. Considering that the lattice constants and thermal expansion coefficients of silicene, germanene, and stanene are different, it is better to use the same kinds of material to realize the functions of *n*-type and *p*-type MOS transistors. Finally, we now discuss an effective way to reduce the threshold light parameter of an X ene transistor.

As shown in the schematic illustration in Fig. 4(a), back gates are added to the light-irradiated regions. It can be seen from Fig. 4(b), in which $|\lambda_{\Omega}| = \lambda_E = 3\lambda_{\text{SO}}^X/4$, that, under the combined action of light and electric fields, a transistor effect can be realized under weak-light-field conditions ($\lambda_{\Omega} < \lambda_{\text{SO}}^X$). The *on* state of the spin-field transistor can be switched to the *off* state as long as $|\lambda_{\Omega}| + |\lambda_E| > \lambda_{\text{SO}}^X$ [red and blue regions in Fig. 4(c)], and the breakdown voltage of the transistor can reach approximately $2[\lambda_{\text{SO}}^X - |\lambda_{\Omega}| - |\lambda_E|]$. It is worth emphasizing that the current cutoff mechanism of the transistor is completely different under different conditions of the light field and staggered potential. By selecting parameters from the red region in Fig. 4(c), the X ene can be transformed into a photoinduced spin-polarized quantum Hall insulator. When $\lambda_{\Omega} > 0$ ($\lambda_{\Omega} < 0$), only spin-down (spin-up) edge states exist in the band gap, and the *off* state of the transistor takes advantage of the mismatch of the spin states. However, the X ene is transformed into a band insulator when the parameters are selected from the blue region, and the transistor utilizes mainly the band gap to block the current. Moreover, for the same reason, the threshold voltage of electrically controlled X ene transistors can be reduced by a light field.

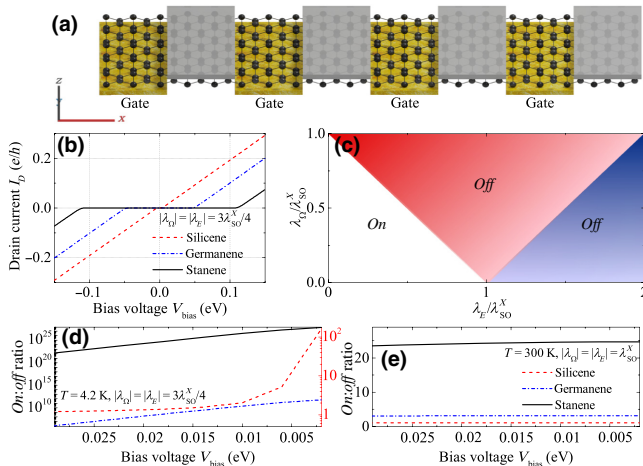


FIG. 4. (a) Schematic illustration of an optically and electrically controlled X ene transistor in which back gates are added to the illuminated regions. (b) Drain current of X ene transistor in the *off* state as a function of the bias voltage V_{bias} with $|\lambda_{\Omega}| = |\lambda_E| = 3\lambda_{\text{SO}}^X/4$. (c) *On* and *off* states of the transistor for different values of the light parameter λ_{Ω} and the staggered potential λ_E . (d) *On:off* ratio of the X ene transistor as a function of the bias voltage V_{bias} at 4.2 K. (e) *On:off* ratio versus V_{bias} with $|\lambda_{\Omega}| = |\lambda_E| = \lambda_{\text{SO}}^X$ at 300 K.

Figures 4(d) and 4(e) depict the *on:off* ratios of transistors jointly controlled by light and electric fields at 4.2 and 300 K. Compared with transistors controlled only by a light field [see Figs. 2(h) and 2(i)], the *on:off* ratio of the silicene, germanene, and stanene transistors is increased obviously by the assistance of the electric field. In particular, as shown in Fig. 4(e), the *off*-state leakage of the stanene transistor at the higher temperature is significantly improved, so that it can maintain a relatively effective *off* state at room temperature. Finally, we would like to discuss the dependence of the *on:off* ratio on the bias voltage. Because the *off* state of the optically controlled transistors studied in this paper is based on a mismatch of energy bands in different regions, the transmission coefficient of electrons can be adjusted to a very small value within the edge-state region, but it is not equal to zero. The closer the electronic energy is to zero, the higher the degree of band mismatch. Therefore, the *off*-state leakage current decreases, and the *on:off* ratio increases with a decrease in the bias voltage.

IV. CONCLUSIONS

In conclusion, we study theoretically the electron transport properties of X ene nanoribbons, in which the central device region is subjected to left- and/or right-circularly-polarized light. It is found that the transistors considered can be switched between a conductive and a nonconductive state by tuning only the strength and polarization state of the light field. The output current can be modulated to

show the following three different types of behavior. (1) When LCP (RCP) light is applied with a light parameter $\lambda_{\Omega} > \lambda_{\text{SO}}^X$ ($\lambda_{\Omega} < -\lambda_{\text{SO}}^X$), the edge states of the illuminated X ene are converted from having a helical property to having an anisotropic chiral property, and the optical transistor can efficiently filter the spin-down (spin-up) electrons due to the edge-state mismatch between the illuminated and unilluminated regions; the drain current is 100% spin-polarized within a specific bias range. (2) When $|\lambda_{\Omega}| < \lambda_{\text{SO}}^X$ or in the absence of light ($\lambda_{\Omega} = 0$), the current is non-spin-polarized, as a consequence of the helical edge states, and the current intensity in the bulk band gap is approximately twice the current intensity obtained in the case where only LCP or RCP light is applied. (3) When LCP and RCP light with $|\lambda_{\Omega}| > \lambda_{\text{SO}}^X$ is applied simultaneously, the conductive path at the edge between regions I and II is blocked, and the drain current vanishes within the bias window $-|\lambda_{\Omega} - \lambda_{\text{SO}}^X| < V_{\text{bias}} < |\lambda_{\Omega} - \lambda_{\text{SO}}^X|$. In addition, we also find that hybrid modulation is an effective way of decreasing the threshold light parameter (threshold voltage) and increasing the breakdown voltage of an optically (electrically) controlled X ene transistor. Under the combined action of light and electric fields, the transistor can be switched off as long as $|\lambda_{\Omega}| + |\lambda_E| > \lambda_{\text{SO}}^X$, and the breakdown voltage of the transistor can reach approximately $2[\lambda_{\text{SO}}^X - |\lambda_{\Omega}| - |\lambda_E|]$. The application of a gate voltage and an increase in the length of the periodic light-receiving structure can effectively improve the *on:off* ratio of the device.

ACKNOWLEDGMENTS

This work was supported by the National Natural Science Foundation of China (Grants No. 11604021, No. 11547209, and No. 11574173) and the Open Project of the State Key Laboratory of Low-Dimensional Quantum Physics (Grant No. KF201910).

- [1] K. S. Novoselov, A. K. Geim, S. V. Morozov, D. Jiang, Y. Zhang, S. V. Dubonos, I. V. Grigorieva, and A. A. Firsov, Electric field effect in atomically thin carbon films, *Science* **306**, 666 (2004).
- [2] K. S. Novoselov, V. I. Falko, L. Colombo, P. R. Gellert, M. G. Schwab, and K. Kim, A roadmap for graphene, *Nature (London)* **490**, 192 (2012).
- [3] S. Manzeli, D. Ovchinnikov, D. Pasquier, O. V. Yazyev, and A. Kis, 2D transition metal dichalcogenides, *Nat. Rev. Mater.* **2**, 17033 (2017).
- [4] K. Takeda and K. Shiraishi, Theoretical possibility of stage corrugation in Si and Ge analogs of graphite, *Phys. Rev. B* **50**, 14916 (1994).
- [5] G. G. Guzman-Verri and L. C. Lew-Yan-Voon, Electronic structure of silicon-based nanostructures, *Phys. Rev. B* **76**, 075131 (2007).

- [6] S. Lebegue and O. Eriksson, Electronic structure of two-dimensional crystals from ab initio theory, *Phys. Rev. B* **79**, 115409 (2009).
- [7] S. Cahangirov, M. Topsakal, E. Akturk, H. Sahin, and S. Ciraci, Two- and One-Dimensional Honeycomb Structures of Silicon and Germanium, *Phys. Rev. Lett.* **102**, 236804 (2009).
- [8] H. Sahin, S. Cahangirov, M. Topsakal, E. Bekaroglu, E. Akturk, R. T. Senger, and S. Ciraci, Monolayer honeycomb structures of group-IV elements and III-V binary compounds: First-principles calculations, *Phys. Rev. B* **80**, 155453 (2009).
- [9] C. C. Liu, W. Feng, and Y. Yao, Quantum Spin Hall Effect in Silicene and Two-Dimensional Germanium, *Phys. Rev. Lett.* **107**, 076802 (2011).
- [10] Y. Xu, B. Yan, H. J. Zhang, J. Wang, G. Xu, P. Tang, W. Duan, and S. C. Zhang, Large-Gap Quantum Spin Hall Insulators in tin Films, *Phys. Rev. Lett.* **111**, 136804 (2013).
- [11] D. Chiappe, C. Grazianetti, G. Tallarida, M. Fanciulli, and A. Molle, Local electronic properties of corrugated silicene phases, *Adv. Mater.* **24**, 5088 (2012).
- [12] A. Fleurence, R. Friedlein, T. Ozaki, H. Kawai, Y. Wang, and Y. Yamada-Takamura, Experimental Evidence for Epitaxial Silicene on Diboride Thin Films, *Phys. Rev. Lett.* **108**, 245501 (2012).
- [13] L. Meng, Y. L. Wang, L. Z. Zhang, S. X. Du, R. T. Wu, L. F. Li, Y. Zhang, G. Li, H. T. Zhou, W. A. Hofer, and H. J. Gao, Buckled silicene formation on Ir (111), *Nano Lett.* **13**, 685 (2013).
- [14] D. Chiappe, E. Scalise, E. Cinquanta, C. Grazianetti, B. van den Broek, M. Fanciulli, M. Houssa, and A. Molle, Two-dimensional Si nanosheets with local hexagonal structure on a MoS₂ surface, *Adv. Mater.* **26**, 2096 (2014).
- [15] M. Derivaz, D. Dentel, R. Stephan, M. C. Hanf, A. Mehdaoui, P. Sonnet, and C. Pirri, Continuous germanene layer on Al (111), *Nano Lett.* **15**, 2510 (2015).
- [16] L. Zhang, P. Bampoulis, A. N. Rudenko, Q. Yao, A. van-Houselt, B. Poelsema, M. I. Katsnelson, and H. J. W. Zandvliet, Structural and Electronic Properties of Germanene on MoS₂, *Phys. Rev. Lett.* **116**, 256804 (2016).
- [17] F. Zhu, W. Chen, Y. Xu, C. Gao, D. Guan, C. Liu, D. Qian, S. Zhang, and J. Jia, Epitaxial growth of two-dimensional stanene, *Nat. Mater.* **14**, 1020 (2015).
- [18] A. Molle, J. Goldberger, M. Houssa, Y. Xu, S. C. Zhang, and D. Akinwande, Buckled two-dimensional Xene sheets, *Nat. Mater.* **16**, 163 (2017).
- [19] Y. F. Ren, Z. H. Qiao, and Q. Niu, Topological phases in two-dimensional materials: A review, *Rep. Prog. Phys.* **79**, 066501 (2016).
- [20] M. Z. Hasan and C. L. Kane, Colloquium: Topological insulators, *Rev. Mod. Phys.* **82**, 3045 (2010).
- [21] X. L. Qi and S. C. Zhang, Topological insulators and superconductors, *Rev. Mod. Phys.* **83**, 1057 (2011).
- [22] M. Ezawa, Monolayer topological insulators: Silicene, germanene, and stanene, *J. Phys. Soc. Jpn.* **84**, 121003 (2015).
- [23] Y. Li, J. Y. Zhang, B. Zhao, Y. Xue, and Z. Q. Yang, Constructive coupling effect of topological states and topological phase transitions in plumbene, *Phys. Rev. B* **99**, 195402 (2019).
- [24] N. D. Drummond, V. Zolyomi, and V. I. Falko, Electrically tunable band gap in silicene, *Phys. Rev. B* **85**, 075423 (2012).
- [25] Z. Ni, Q. Liu, K. Tang, J. Zheng, J. Zhou, R. Qin, Z. Gao, D. Yu, and J. Lu, Tunable bandgap in silicene and germanene, *Nano Lett.* **12**, 113 (2012).
- [26] J. S. Qi, K. G. Hu, and X. Li, Electric control of the edge magnetization in zigzag stanene nanoribbons from first principles, *Phys. Rev. Appl.* **10**, 034048 (2018).
- [27] C. H. Chen, W. W. Li, Y. M. Chang, C. Y. Lin, S. H. Yang, Y. Xu, and Y. F. Lin, Negative-differential-resistance devices achieved by band-structure engineering in silicene under periodic potentials, *Phys. Rev. Appl.* **10**, 044047 (2018).
- [28] M. Ezawa, Quantized conductance and field-effect topological quantum transistor in silicene nanoribbons, *Appl. Phys. Lett.* **102**, 172103 (2013).
- [29] G. L. Lay, 2D materials: Silicene transistors, *Nat. Nanotech.* **10**, 202 (2015).
- [30] L. Tao, E. Cinquanta, D. Chiappe, C. Grazianetti, M. Fanciulli, M. Dubey, A. Molle, and D. Akinwande, Silicene field-effect transistors operating at room temperature, *Nat. Nanotech.* **10**, 227 (2015).
- [31] Y. Wang, Z. Ni, Q. Liu, R. Quhe, J. Zheng, M. Ye, D. Yu, J. Shi, J. Yang, J. Li, and J. Lu, All-metallic vertical transistors based on stacked Dirac materials, *Adv. Funct. Mater.* **25**, 68 (2015).
- [32] B. N. Madhushankar, A. Kaverzin, T. Giousis, G. Potsi, D. Gournis, P. Rudolf, G. R. Blake, C. H. van der Wal, and B. J. van-Wees, Electronic properties of germanane field-effect transistors, *2D Mater.* **4**, 021009 (2017).
- [33] Y. Xu, Y. R. Chen, J. Wang, J. F. Liu, and Z. S. Ma, Quantized Field-Effect Tunneling between Topological Edge or Interface States, *Phys. Rev. Lett.* **123**, 206801 (2019).
- [34] Y. Katayama, R. Yamauchi, Y. Yasutake, S. Fukatsu, and K. Ueno, Ambipolar transistor action of germanane electric double layer transistor, *Appl. Phys. Lett.* **115**, 122101 (2019).
- [35] X. L. Lv and H. Xie, Spin filters and switchers in topological-insulator junctions, *Phys. Rev. Appl.* **12**, 064040 (2019).
- [36] J. Bardeen and W. H. Brattain, The transistor, a semiconductor triode, *Phys. Rev.* **74**, 230 (1948).
- [37] M. Lundstrom, Moore's law forever? *Science* **299**, 210 (2003).
- [38] M. M. Waldrop, More than Moore, *Nature (London)* **530**, 145 (2016).
- [39] D. A. B. Miller, Device requirements for optical interconnects to silicon chips, *Proc. IEEE* **97**, 1166 (2009).
- [40] H. Chang, Z. Sun, Q. Yuan, F. Ding, X. Tao, F. Yan, and Z. Zheng, Thin film field-effect phototransistors from bandgap-tunable, solution-processed, few-layer reduced graphene oxide films, *Adv. Mater.* **22**, 4872 (2010).
- [41] W. Zhang, J. K. Huang, C. H. Chen, Y. H. Chang, Y. J. Cheng, and L. J. Li, High-gain phototransistors based on a CVD MoS₂ monolayer, *Adv. Mater.* **25**, 3456 (2013).
- [42] T. Low, M. Engel, M. Steiner, and P. Avouris, Origin of photoresponse in black phosphorus phototransistors, *Phys. Rev. B* **90**, 081408(R) (2014).

- [43] H. Xu, J. Wu, Q. Feng, N. Mao, C. Wang, and J. Zhang, High responsivity and gate tunable graphene-MoS₂ hybrid phototransistor, *Small* **10**, 2300 (2014).
- [44] L. Tu, R. Cao, X. Wang, Y. Chen, S. Wu, F. Wang, Z. Wang, H. Shen, T. Lin, P. Zhou, X. Meng, W. Hu, Q. Liu, J. Wang, M. Liu, and J. Chu, Ultrasensitive negative capacitance phototransistors, *Nat. Commun.* **11**, 1 (2020).
- [45] C. L. Kane and E. J. Mele, Z₂ Topological Order and the Quantum Spin Hall Effect, *Phys. Rev. Lett.* **95**, 146802 (2005).
- [46] C. C. Liu, H. Jiang, and Y. Yao, Low-energy effective Hamiltonian involving spin-orbit coupling in silicene and two-dimensional germanium and tin, *Phys. Rev. B* **84**, 195430 (2011).
- [47] M. Ezawa, Valley-Polarized Metals and Quantum Anomalous Hall Effect in Silicene, *Phys. Rev. Lett.* **109**, 055502 (2012).
- [48] J. Zheng, F. Chi, and Y. Guo, Thermal spin generator based on a germanene nanoribbon subjected to local noncollinear exchange fields, *Phys. Rev. Appl.* **9**, 024012 (2018).
- [49] J. Zheng, F. Chi, and Y. Guo, Spin-current diodes based on germanene and stanene subjected to local exchange fields, *Appl. Phys. Lett.* **113**, 112404 (2018).
- [50] F. D. M. Haldane, Model for a Quantum Hall Effect Without Landau Levels: Condensed-Matter Realization of the “Parity Anomaly”, *Phys. Rev. Lett.* **61**, 2015 (1988).
- [51] C. L. Kane and E. J. Mele, Quantum Spin Hall Effect in Graphene, *Phys. Rev. Lett.* **95**, 226801 (2005).
- [52] M. Ezawa, Photoinduced Topological Phase Transition and a Single Dirac-Cone State in Silicene, *Phys. Rev. Lett.* **110**, 026603 (2013).
- [53] T. Oka and H. Aoki, Photovoltaic Hall effect in graphene, *Phys. Rev. B* **79**, 081406(R) (2009).
- [54] T. Kitagawa, T. Oka, A. Brataas, L. Fu, and E. Demler, Transport properties of nonequilibrium systems under the application of light: Photoinduced quantum Hall insulators without Landau levels, *Phys. Rev. B* **84**, 235108 (2011).
- [55] Y. Meir and N. S. Wingreen, Phys, *Rev. Lett.* **68**, 2512 (1992).
- [56] S. Datta, *Electronic Transport in Mesoscopic Systems* (Cambridge University Press, New York, 1995).
- [57] D. H. Lee and J. D. Joannopoulos, Simple scheme for surface-band calculations. I, *Phys. Rev. B* **23**, 4988 (1981).
- [58] D. H. Lee and J. D. Joannopoulos, Simple scheme for surface-band calculations. II. The Green’s function, *Phys. Rev. B* **23**, 4997 (1981).
- [59] S. Groenendijk, G. Dolcetto, and T. L. Schmidt, Fundamental limits to helical edge conductivity due to spin-phonon scattering, *Phys. Rev. B* **97**, 241406 (2018).
- [60] S. Q. Chen, Z. C. Li, W. W. Liu, H. Cheng, and J. G. Tian, From single-dimensional to multidimensional manipulation of optical waves with metasurfaces, *Adv. Mater.* **31**, 1802458 (2019).
- [61] S. M. Sze, *Physics of Semiconductor Devices: Physics and Technology* (Wiley, New York, 2001), 2nd ed.
- [62] D. K. Schröder, *Semiconductor Material and Device Characterization* (Wiley, New York, 2006).